Electronic Supplementary Material (ESI) for Journal of Materials Chemistry B.

Supporting Information

Photocleavable core cross-linked polymeric micelles of polypept(o)ides and ruthenium(II) complexes

Tobias Alexander Bauer,[a,b] Jonas Eckrich,[c,d] Nadine Wiesmann,[c] Felix Kuczelinis,[b] Wen Sun,[e] Xiaolong Zeng,[e] Benjamin Weber,[b] Si Wu,[e] Nicolas Hubert Bings,[b] Sebastian Strieth,[c,d] Matthias Barz *[a,b]

[a] TA. Bauer, Prof. Dr. M. Barz*
Leiden Academic Centre for Drug Research (LACDR)
Leiden University
Einsteinweg 55, 2333CC Leiden, The Netherlands
E-mail: m.barz@lacdr.leidenuniv.nl

[b] TA. Bauer, Dr. B. Weber, F. Kuczelinis, Prof. Dr. NH. Bings, Prof. Dr. M. Barz
Department of Chemistry
Johannes Gutenberg University Mainz
Duesbergweg 10-14, 55128 Mainz, Germany

[c] Dr. J. Eckrich, Dr. N. Wiesmann, Prof. Dr. S. Strieth
Department of Otorhinolaryngology, Head and Neck Surgery
University Medical Center Mainz
Langenbeckstr. 1, 55131 Mainz, Germany

[d] Dr. J. Eckrich, Prof. Dr. S. Strieth
Department of Otorhinolaryngology
University Hospital Bonn
Venusberg-Campus 1, 53127 Bonn, Germany

[e] X. Zeng, Dr. W. Sun, Dr. S. Wu
Max Planck Institute for Polymer Research
Ackermannweg 10, 55128 Mainz, Germany

Table of Contents

Results and Discussion

Polymer Synthesis

Table S1. Analytical results of the polymer synthesis of **P1** to **P9.**

polymer	*M/I (calc.)*	X_n (pGlu)[a]	X_n (pSar)[b]	M_n [c] / kDa	M_w [c] / kDa	$Đ$ [c]	CN-Graft.[a]
P1, pGlu(O*t*Bu)$_{36}$	30	36	-	19.7	22.9	1.16	
P2, pGlu(O*t*Bu)$_{36}$-*b*-pSar$_{171}$	160	36	171	44.0	52.9	1.20	
P3, pGlu(OH)$_{36}$-*b*-pSar$_{171}$	-	36	171	37.9	59.1	1.56	
P4, pGlu(Mod)$_{36}$-*b*-pSar$_{171}$	-	36	171	53.1	74.8	1.41	52%
P5, *N*-Boc-pSar$_{140}$	200	-	140	-	-	-	-
P6, pSar$_{140}$	-	-	140	28.7	34.5	1.20	-
P7-A, pSar$_{140}$-*b*-pGlu(O*t*Bu)$_{20}$	20	19	140	30.0	39.3	1.31	-
P7-B, pSar$_{140}$-*b*-pGlu(O*t*Bu)$_{15}$	15	14	140	30.3	40.7	1.34	-
P8-A, pSar$_{140}$-*b*-pGlu(OH)$_{20}$	-	19	140	28.2	35.6	1.26	-
P8-B, pSar$_{140}$-*b*-pGlu(OH)$_{15}$	-	14	140	30.9	54.1	1.75	-
P9-A, pSar$_{140}$-*b*-pGlu(Mod)$_{20}$	-	19	140	71.3	113.2	1.58	65%
P9-B, pSar$_{140}$-*b*-pGlu(Mod)$_{15}$	-	14	140	47.9	61.5	1.28	100%

(a) determined by ^{1}H NMR (b) determined by HFIP-GPC with pSar standards. (c) determined by HFIP-GPC with PMMA Standards

HFIP-GPC Analysis

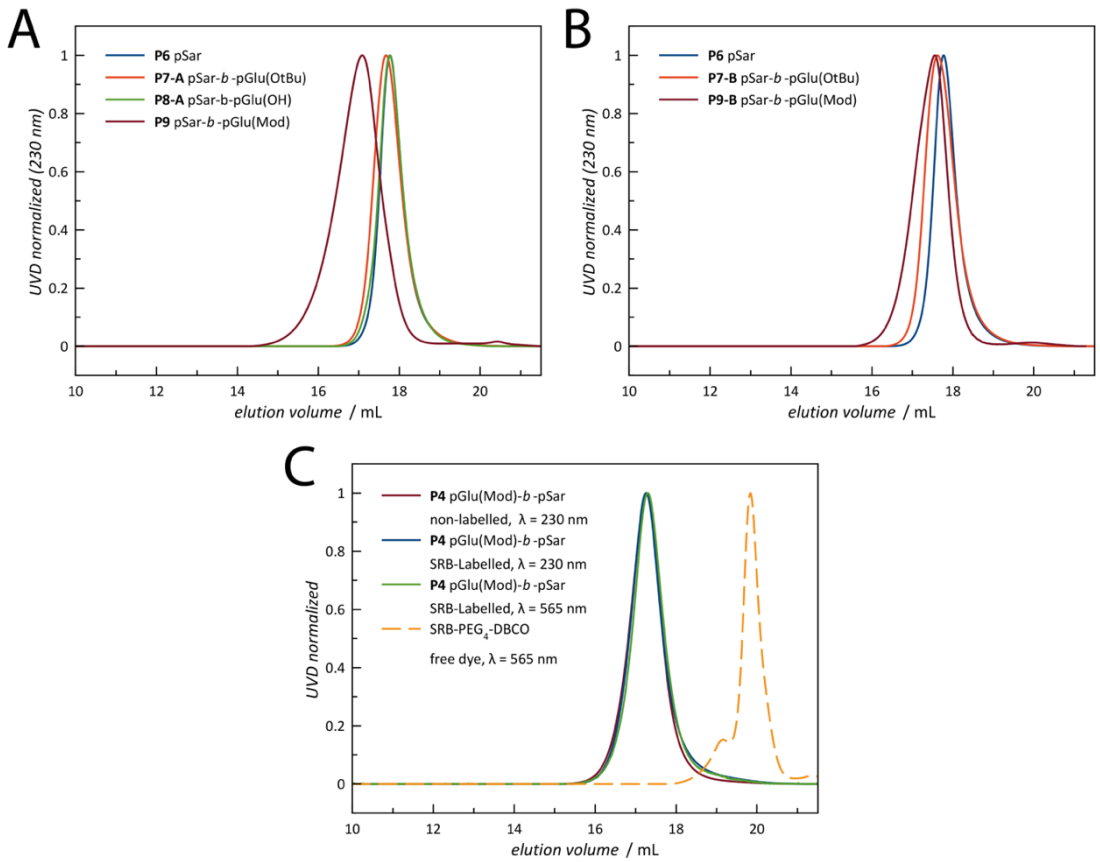

Figure S1. Analytical HFIP GPC. (A) Polymers P6 to P9-A, (B) Polymers P6 to P9-B, (C) Labelling of P4 with Sulforhodamine-B, whereby no free unconjugated dye is detectable.

FT-IR Spectroscopy

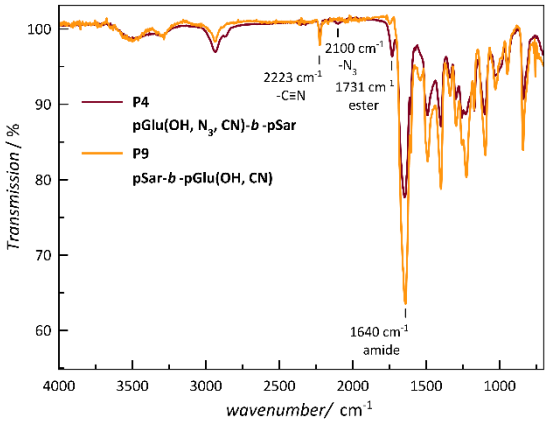

Figure S2. Comparison of cyano-modified polymers P4 (dark red) and P9-A (orange) by FT-IR spectroscopy. As expected, the ester bond is not visible in P9-A, but only in P4.

Photocleavable Core Cross-Linked Polymeric Micelles (PCCPMs)

Images

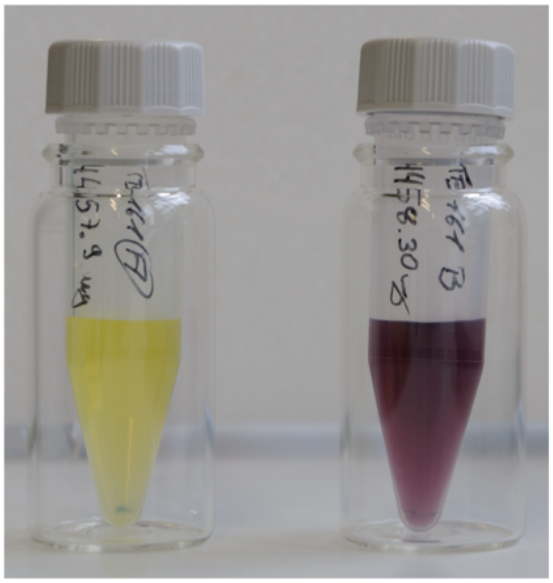

Figure S3. Images of PCCPMs after completed purification by spin-filtration. PCCPM-1 (left) and PCCPM-2 (right).

Multi-Angle Dynamic Light Scattering in Human Plasma

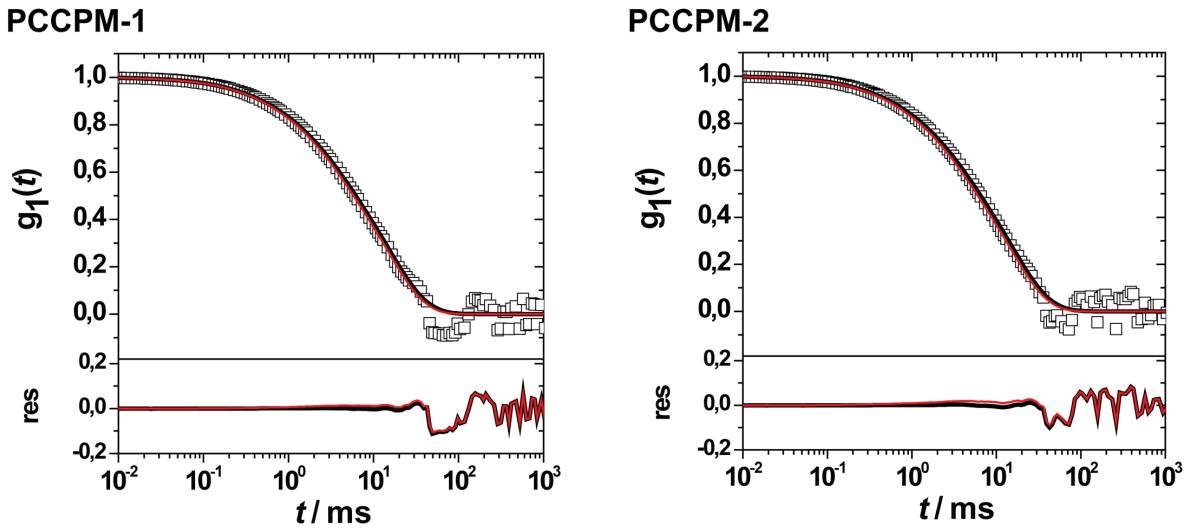

Figure S4. Multi-Angle Dynamic Light Scattering of PCCPM-1 (left) and PCCPM-2 (right) in human plasma.[1] Autocorrelation function $g_1(t)$ for an exemplary scattering angle of 30° for fits with (red) and without (black line) aggregate term (upper graph), and the residuals of fits w/o aggregate and correlation function (lower graph).

Extended TEM Analysis

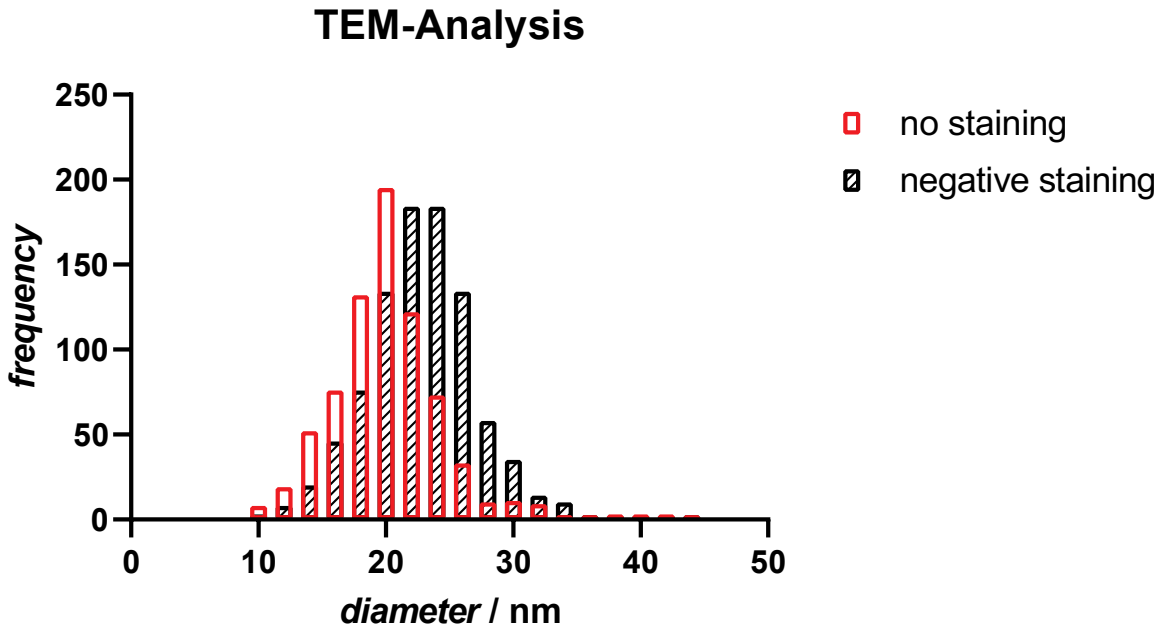

Figure S5. Particle analysis by TEM for PCCPM-2. (red) without staining; average particle diameter of 20.2 ± 4.5 nm, PDI 0.050. (black) negatively stained with uranyl acetate; average particle diameter of 22.8 ± 4.3 nm, PDI 0.034. Objects smaller than 10 nm diameter were excluded for statistics.

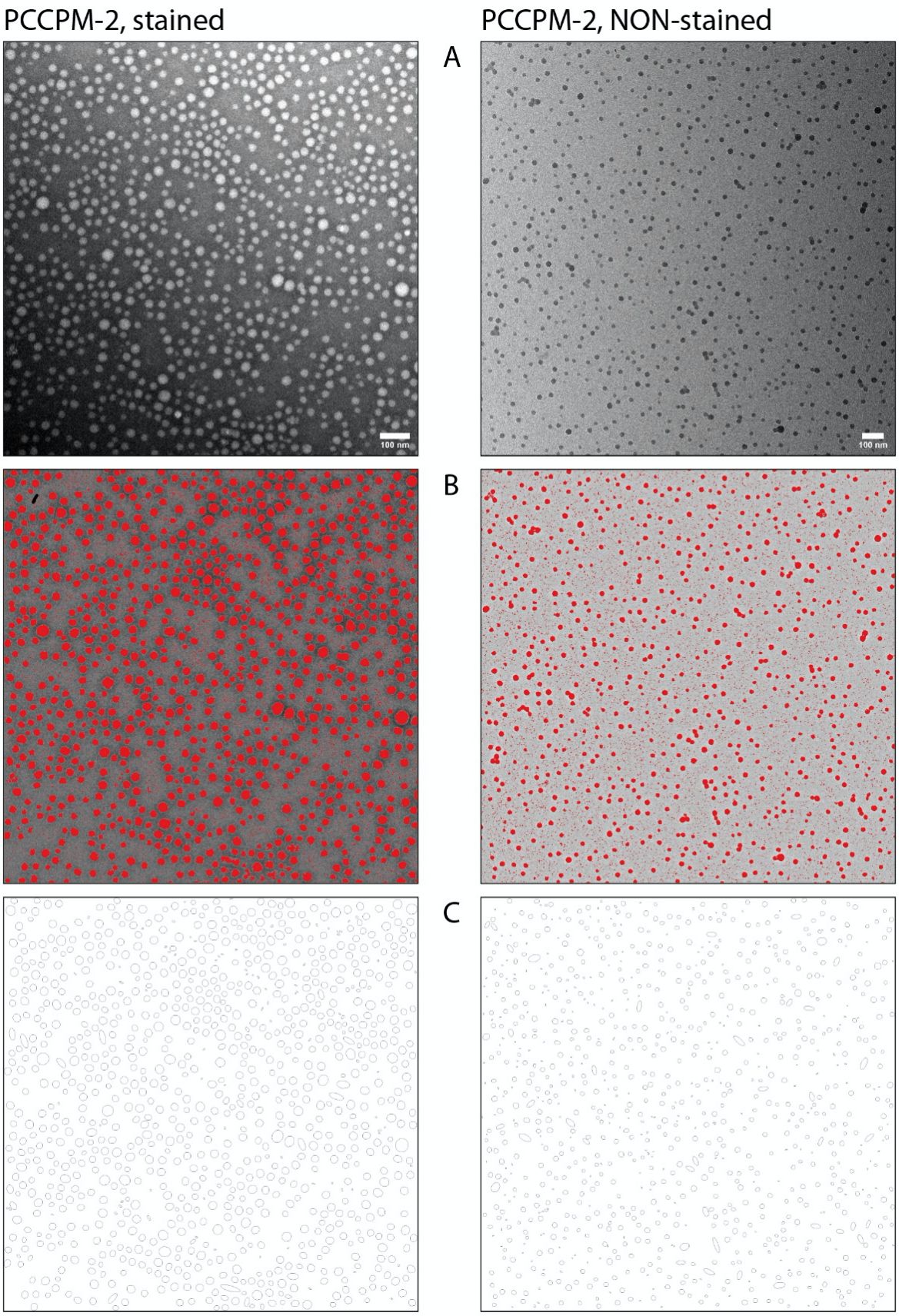

Figure S6. Exemplified particle counting for non-stained (left) and negatively stained samples (right) using ImageJ 1.52h.(A) parent TEM image, (B) derived threshold image, (C) area analysis for given threshold objects. Assuming spherical shape, diameters were calculated for each object.

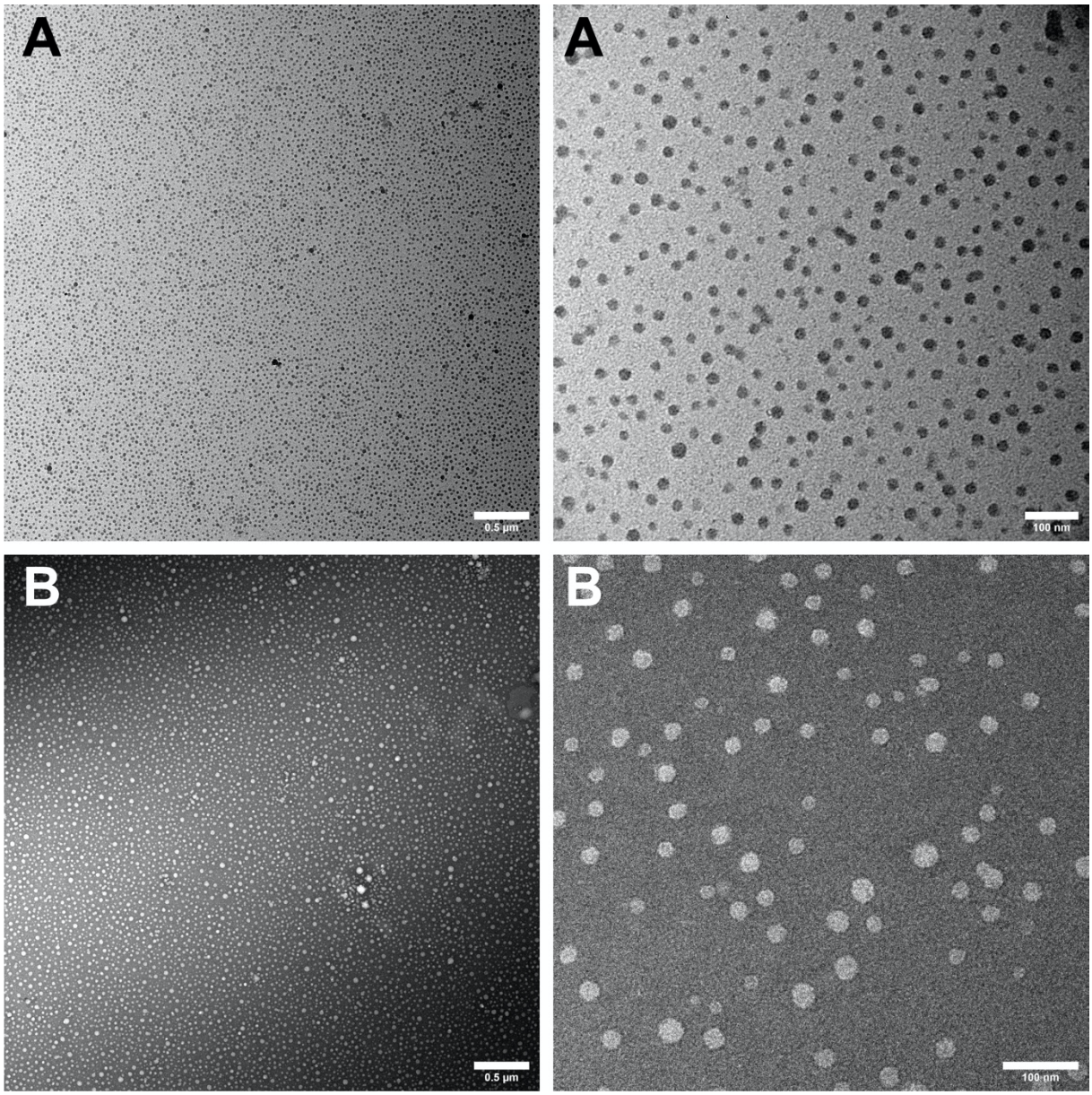

Figure S7. TEM Analysis of PCCPM-1. (A) without staining, (B) negative staining.

Worm-like Photocleavable Core Cross-Linked Polymeric Micelles (w-PCCPM)

Multi-Angle Dynamic Light Scattering of Worm-Like PCCPMs

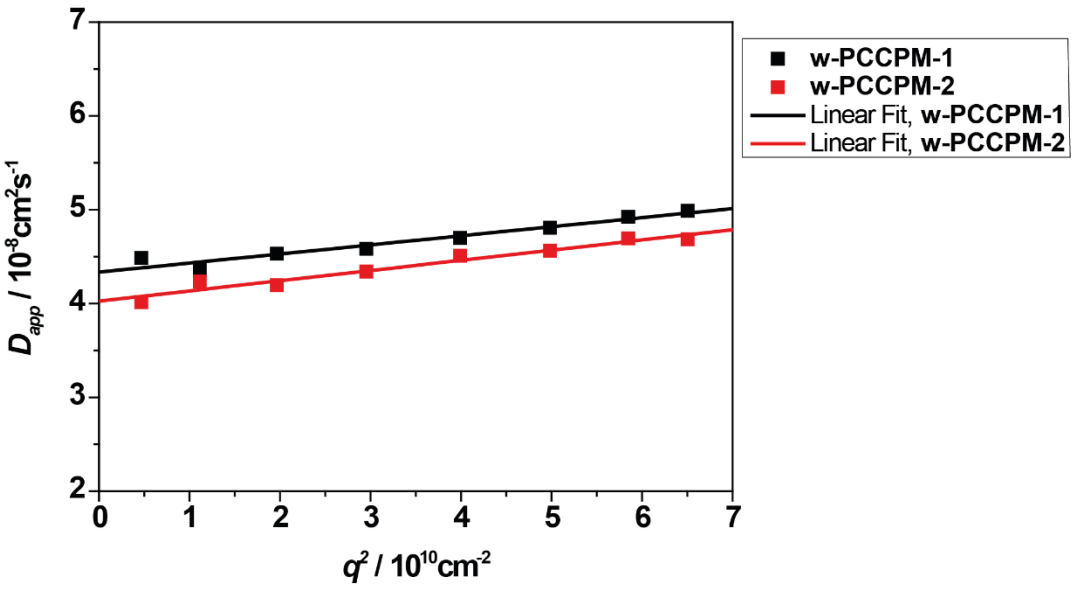

Figure S8. Multi-angle dynamic light scattering of worm-like PCCPMs in PBS prepared from **P9-A**.

AFM Analysis of Worm-Like PCCPMs

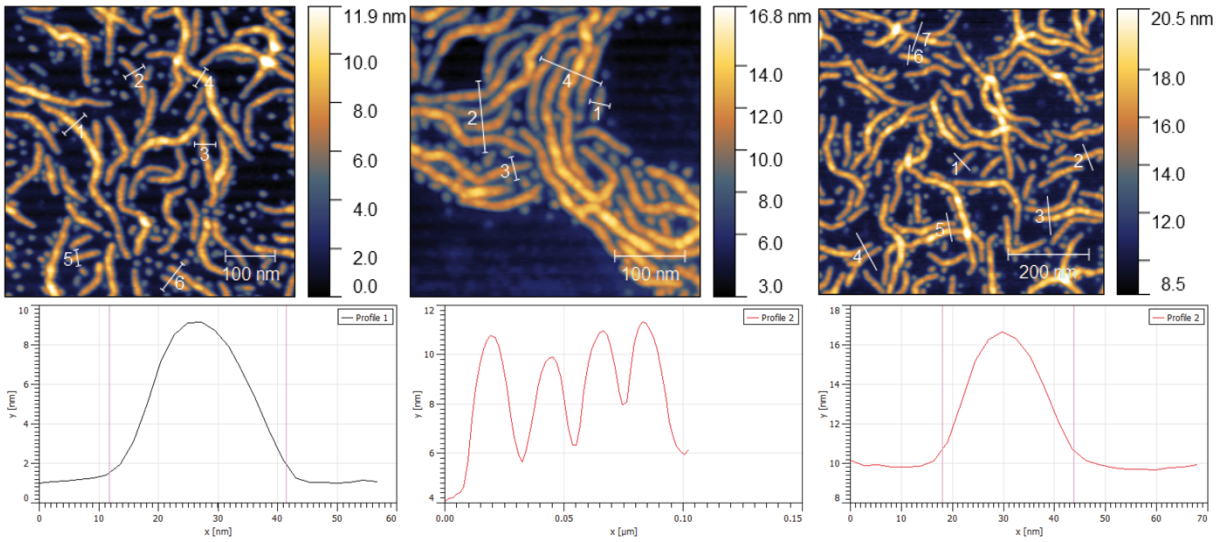

Figure S9. AFM image analysis of w-PCCPM-1. AFM images with indicated profiles (lower) and exemplary apparent height profiles.

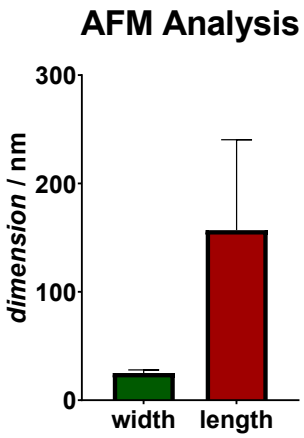

Figure S10. AFM image analysis of w-PCCPM-1. Average rod width 25 ± 3 nm (N = 27); Average rod length 157 ± 83 nm (N = 90).

Block Length Variations for Spherical PCCPMs

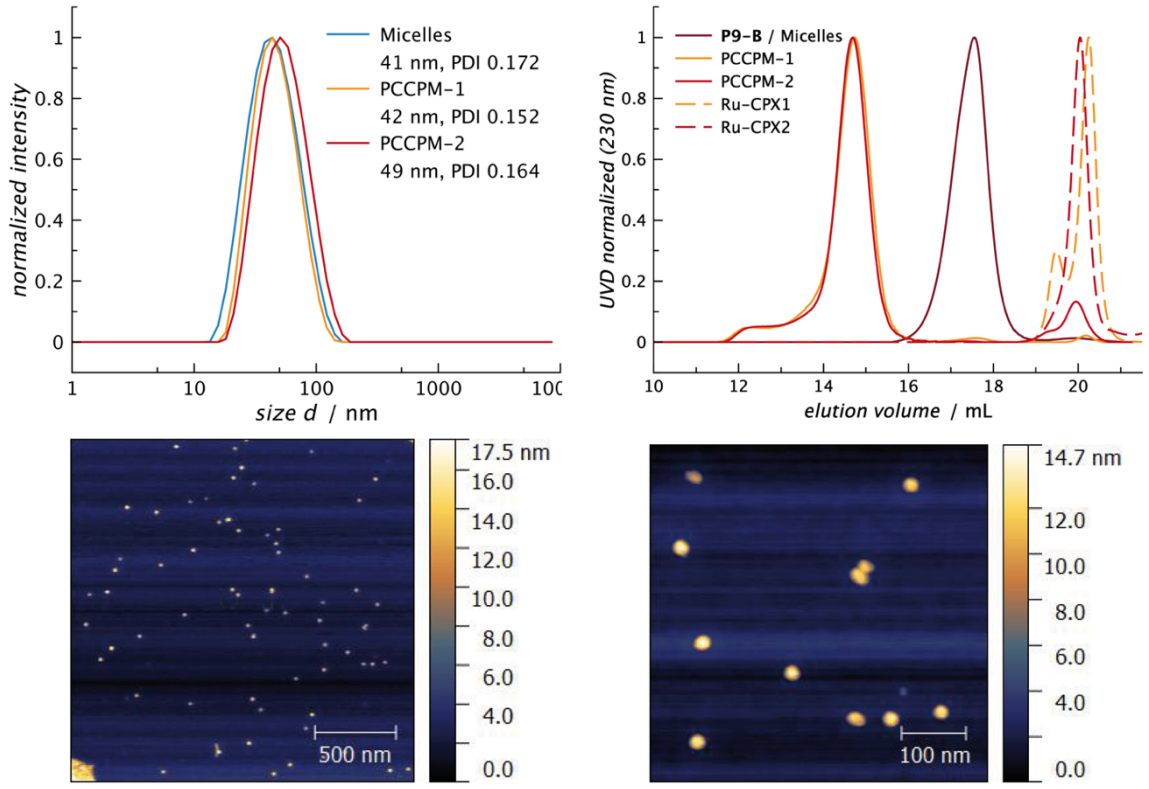

Figure S11. Spherical PCCPMs from amide-modified $pSar_{140}$-*b*-$pGlu_{15}$ block copolymer. Only slight bimodal GPC-trace. PCCPM-2 shows large amounts of non-covalent Ru-CPX-encapsulation, well corresponding with higher drug contents (11.84 wt.%).

Table S2. Characrerization of spherical PCCPMs from $pSar_{140}$-*b*-$pGlu(Mod)_{15}$ (P9-B).

particle	*Ru-CPX*	D_h /nm[a]	*PDI*[a]	D_h /nm[b]	*Ru-CPX-content* / wt.%[c]
Micelles/P9-B	-	41	0.172	-	-
PCCPM-1/P9-B	$[Ru(bpy)_2]^{2+}$	42	0.152	63	3.19 ± 0.25
PCCPM-2/P9-B	$[Ru(biq)_2]^{2+}$	49	0.164	71	11.84 ± 0.93

[a] determined by single-angle dynamic light scattering at an angle of 173°, [b] determined by multi-angle dynamic light scattering, [c] determined by ICP-MS.

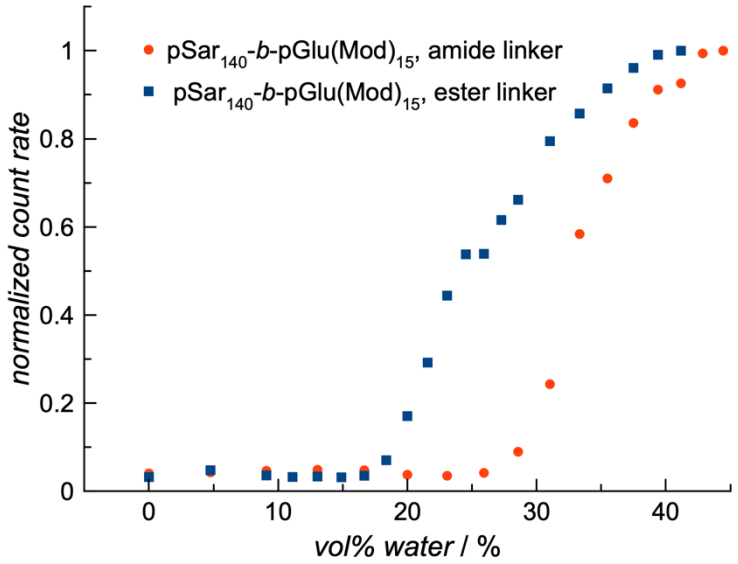

Figure S12. DLS count rate analysis accounts for aggregation of modified $pSar_{140}$-*b*-$pGlu(Mod)_{15}$ copolymers. Copolymers were dissolved in DMSO (5 $g \cdot L^{-1}$) and water was added sequentially.

Photocleavage

UV-Vis Spectroscopy

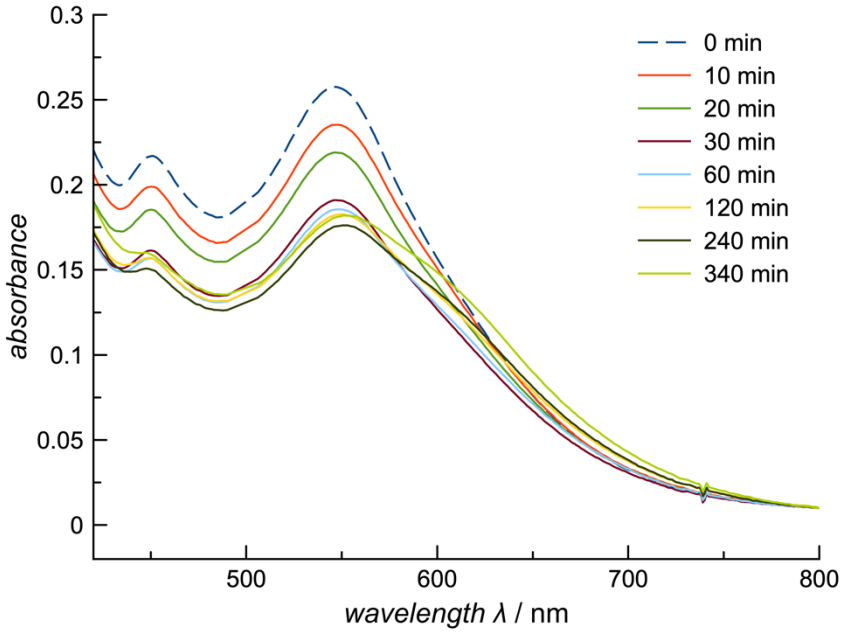

Figure S13. Photocleavage of PCCPM-2 with a red-orange LED (620 nm).

Biological Evaluation

In vitro Studies

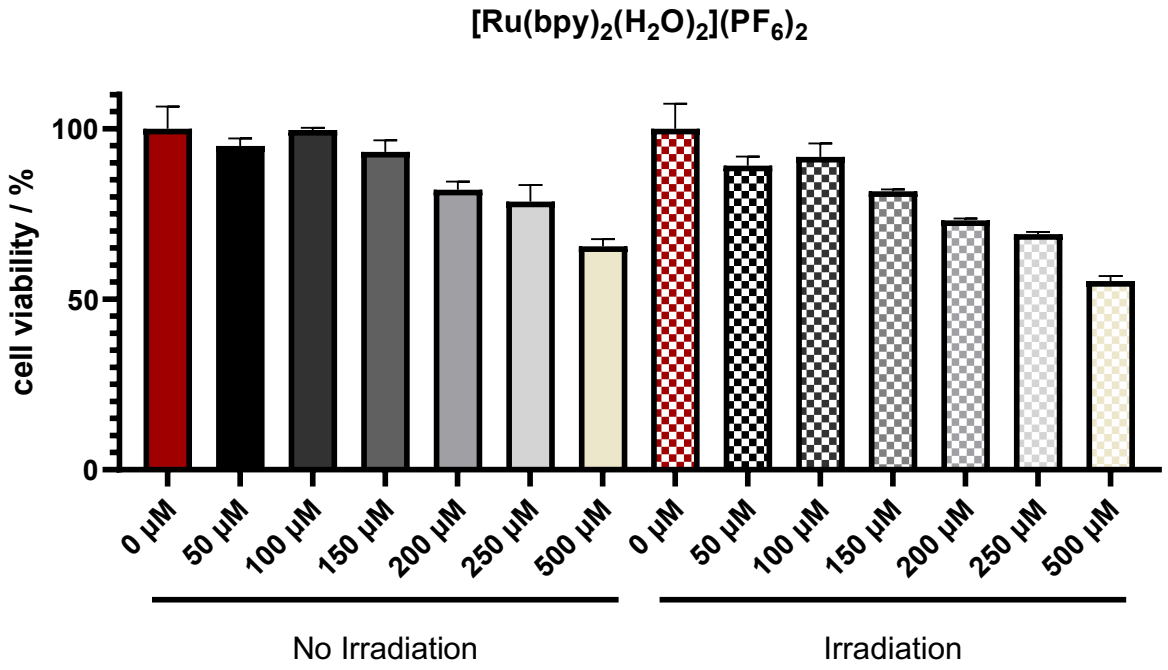

Figure S14. Viability of HuH-7 cells after incubation with Ru-CPX-1 for 24 h with or without irradiation relative to untreated control (0 µM), as analyzed by Alamar Blue Assay.

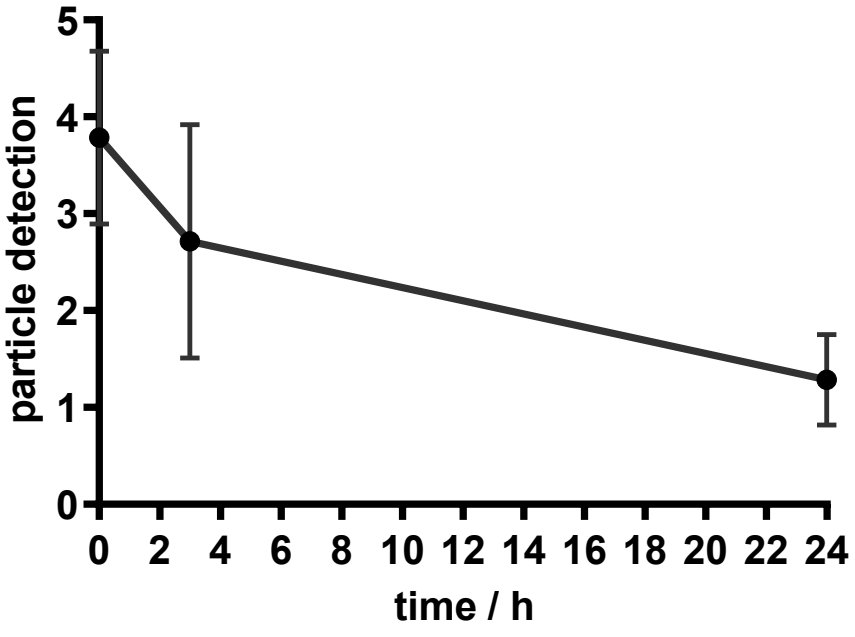

Figure S15. Analysis of intravascular circulation. After intravascular application of the sulforhodamine B labeled nanoparticles, in vivo fluorescent microscopy was performed. After blinding, video sequences were investigated repetitively three times. As the intensity of particles in the vascular system did not allow a sufficient quantitative analysis the following numerical analogue scale was applied:

5 = intravascular nanoparticles can be detected ubiquitously; 4 = intravascular nanoparticles can be detected predominantly; 3 = intravascular nanoparticles can be detected occasionally; 2 = nanoparticles can be detected; 1 = no nanoparticles can be detected. Data shown as Mean + Error.

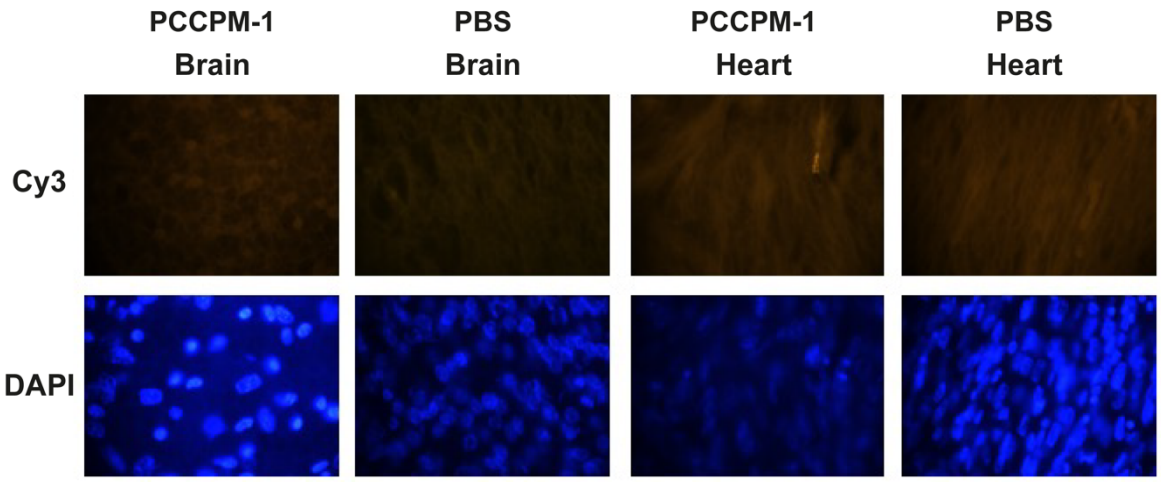

Figure S16. Representative fluorescence microscopy images of brain and heart tissue taken with the Cy3 and DAPI filter after application of sulforhodamine B labeled PCCPM or control (PBS).

References

1 K. Rausch, A. Reuter, K. Fischer and M. Schmidt, *Biomacromolecules*, 2010, **11**, 2836–2839.

Appendix

^{1}H NMR Spectroscopy

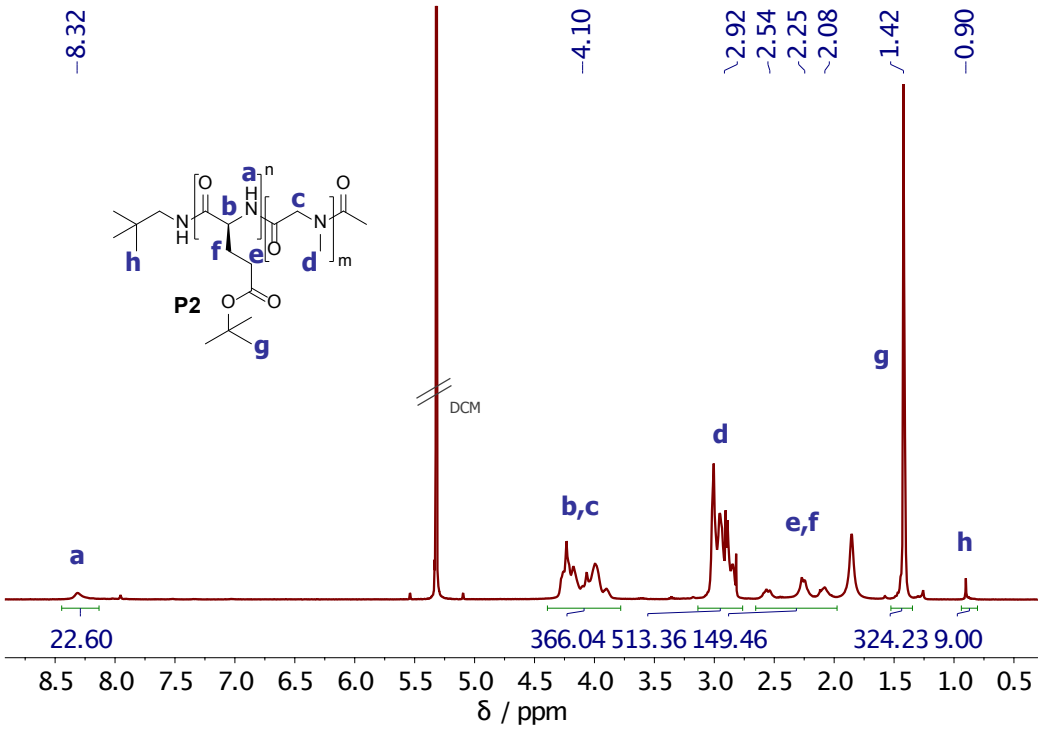

Figure S17. ^{1}H NMR spectrum of **P2** (pGlu(O*t*Bu)$_{36}$-*b*-pSar$_{171}$) in CD_2Cl_2.

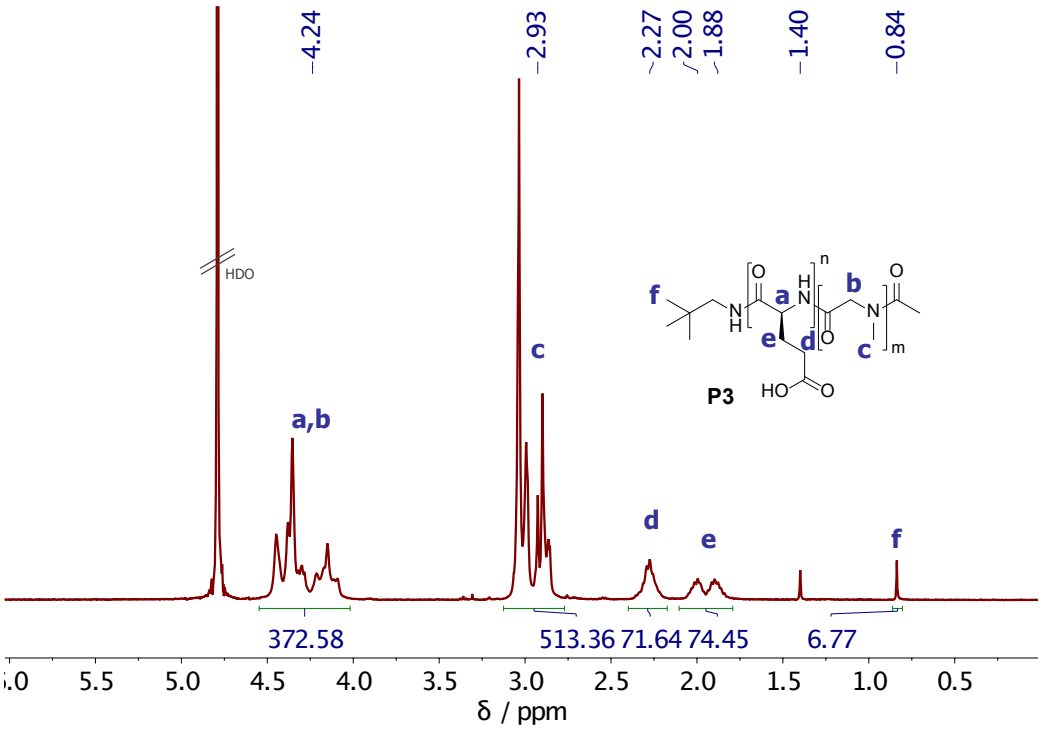

Figure S18. ^{1}H NMR spectrum of **P3** (pGlu(OH)$_{36}$-*b*-pSar$_{171}$) in D_2O.

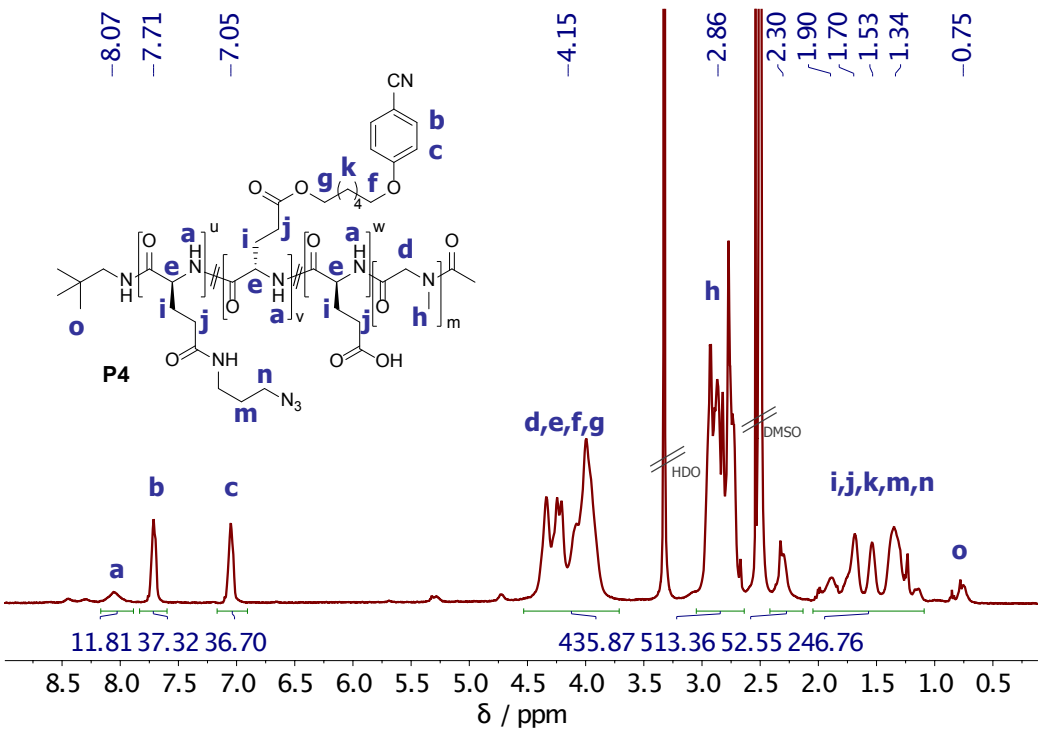

Figure S19. ^{1}H NMR spectrum of **P4** (pGlu(Mod)$_{36}$-*b*-pSar$_{171}$) in DMSO-d_6.

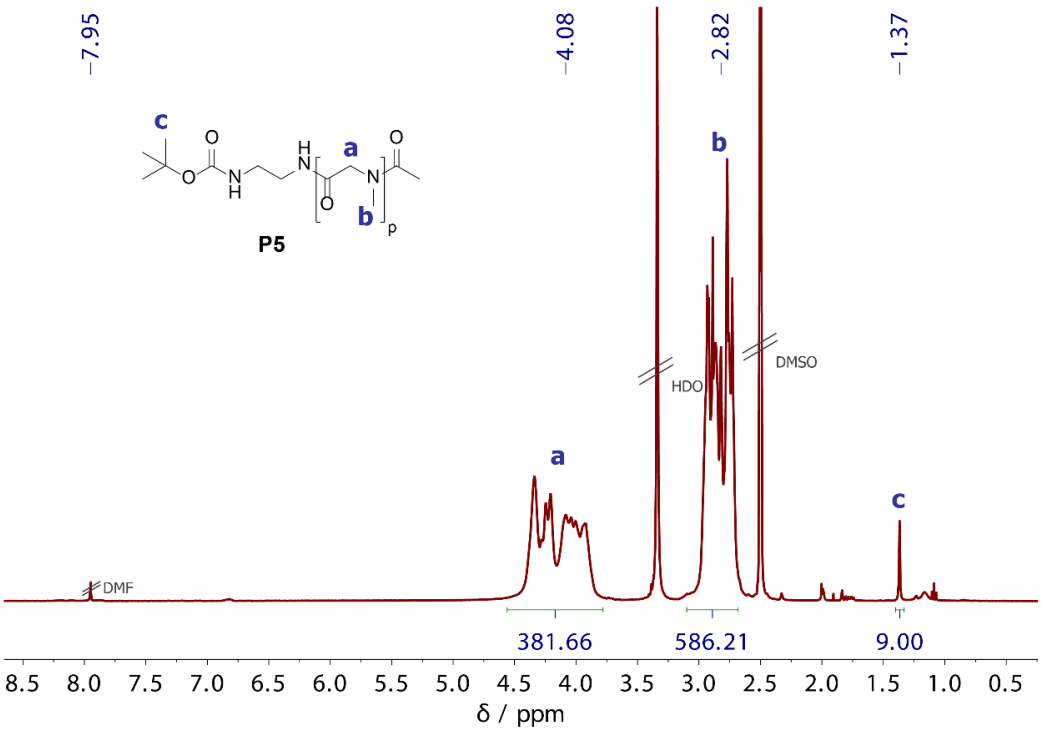

Figure S20. ^{1}H NMR spectrum of **P5** (*N*-Boc-pSar$_{140}$) in DMSO-d_6.

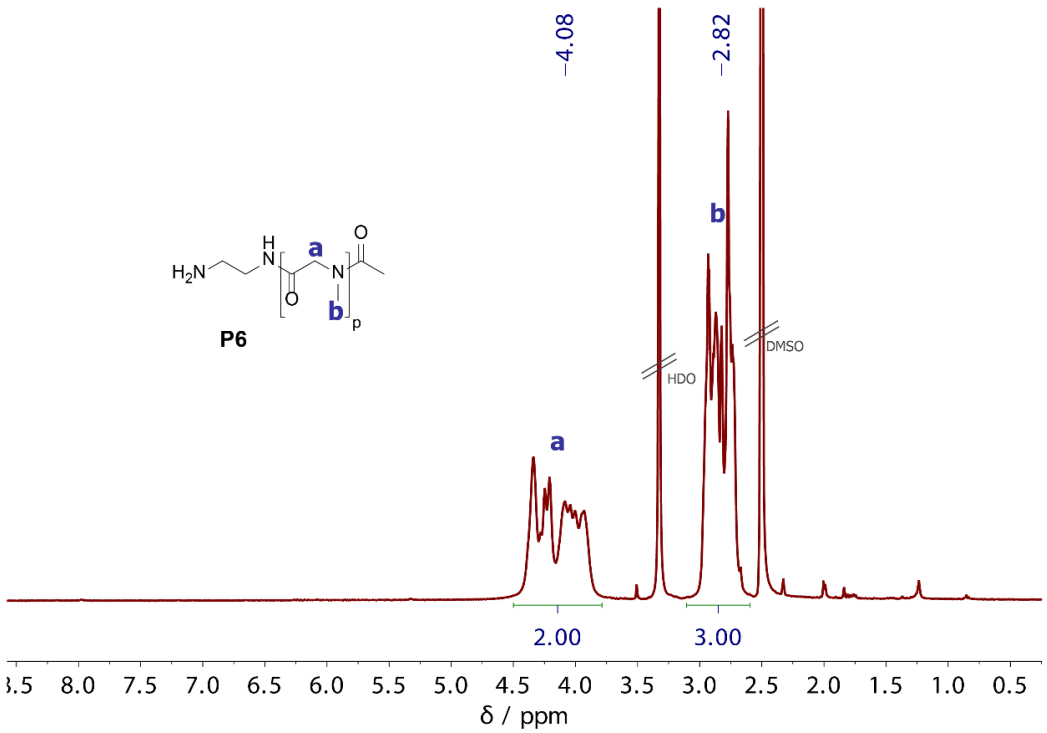

Figure S21. ^{1}H NMR spectrum of **P6** ($pSar_{140}$) in DMSO-d_6.

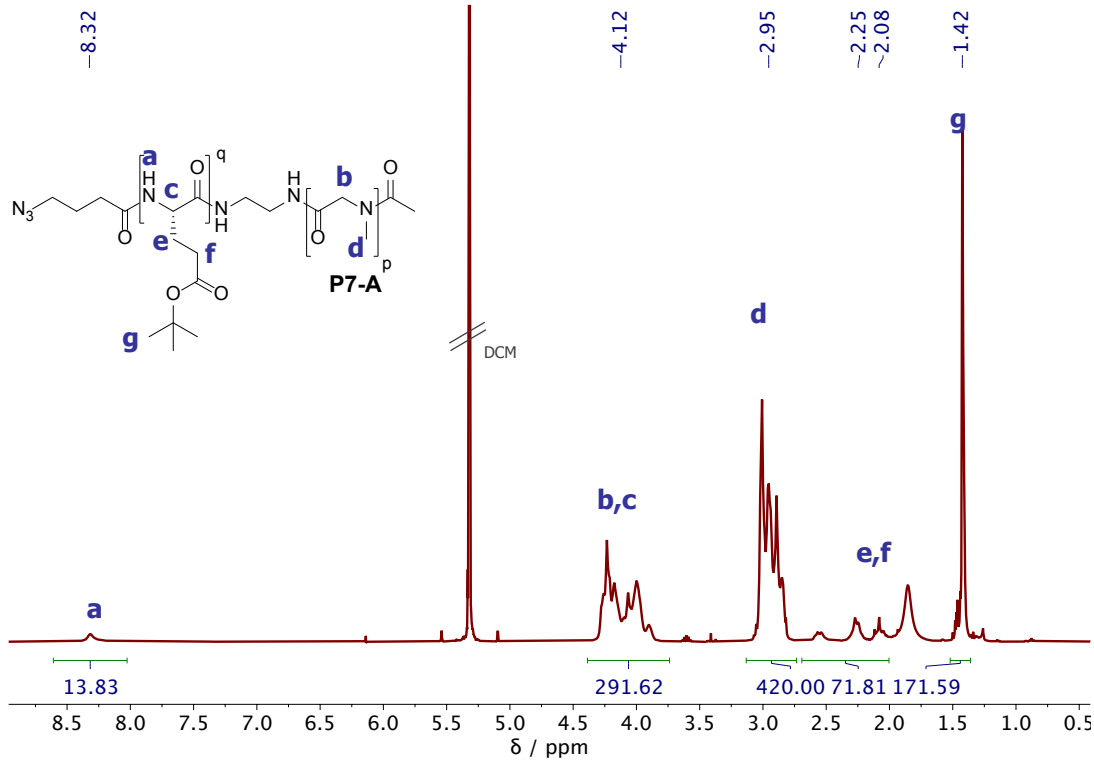

Figure S22. ^{1}H NMR spectrum of **P7-A** ($pSar_{140}$-*b*-pGlu(O*t*Bu)$_{20}$) in CD_2Cl_2.

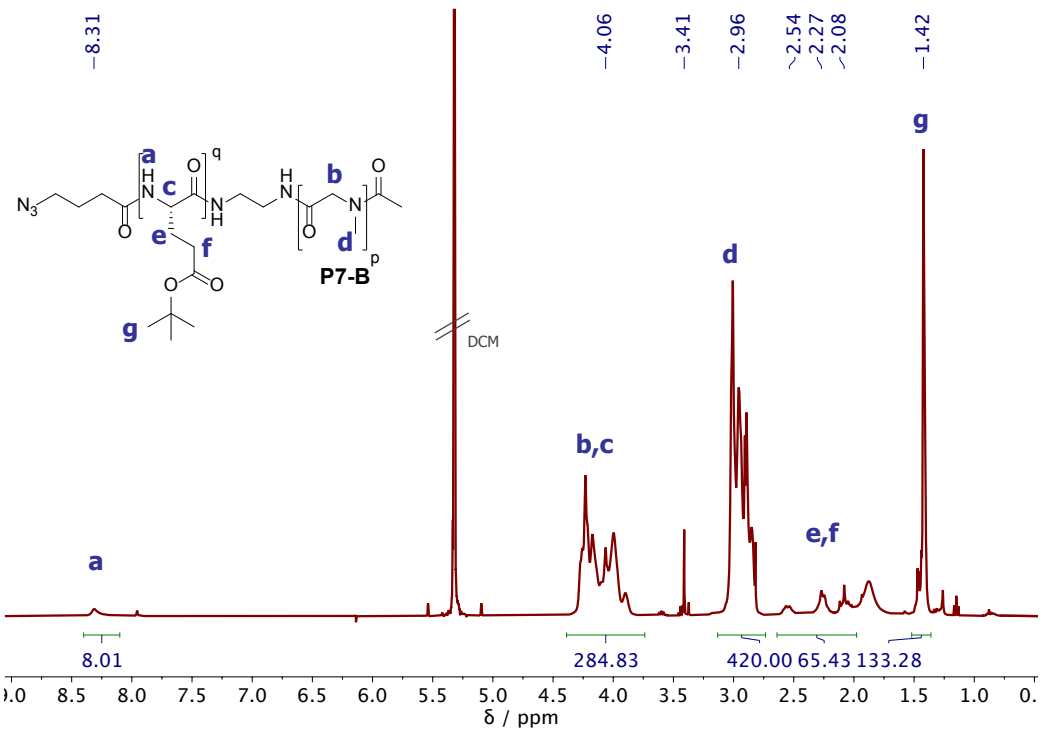

Figure S23. ^{1}H NMR spectrum of **P7-B** ($pSar_{140}$-*b*-$pGlu(O\mathit{t}Bu)_{15}$) in CD_2Cl_2.

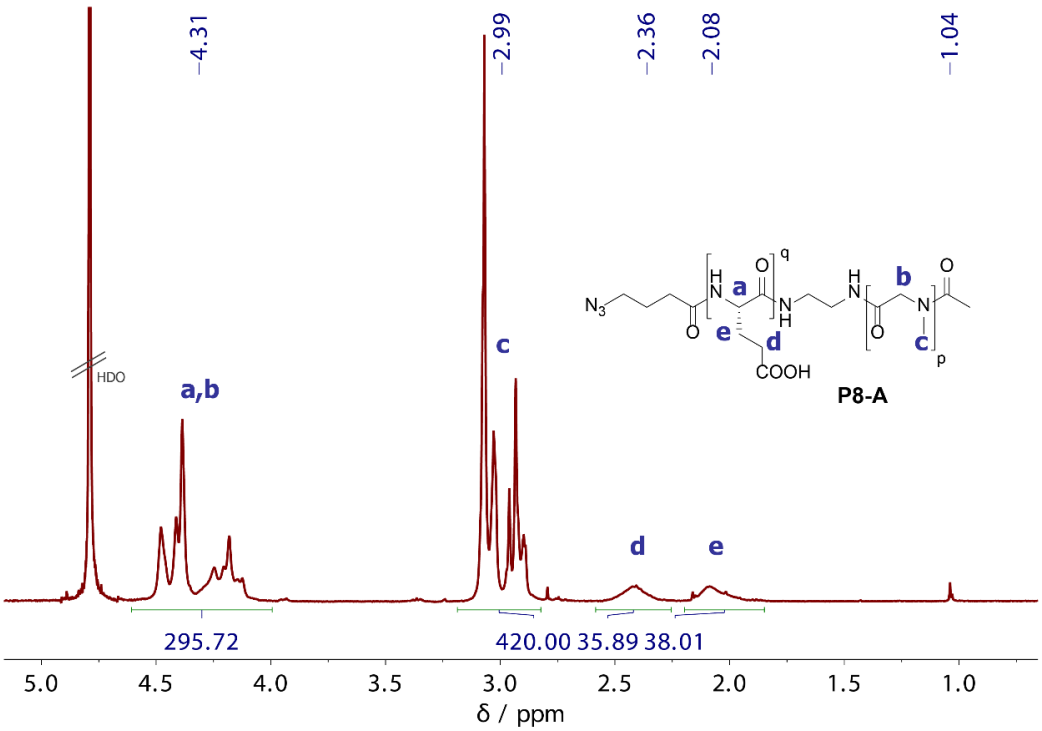

Figure S24. ^{1}H NMR spectrum of **P8-A** ($pSar_{140}$-*b*-$pGlu(OH)_{20}$) in D_2O.

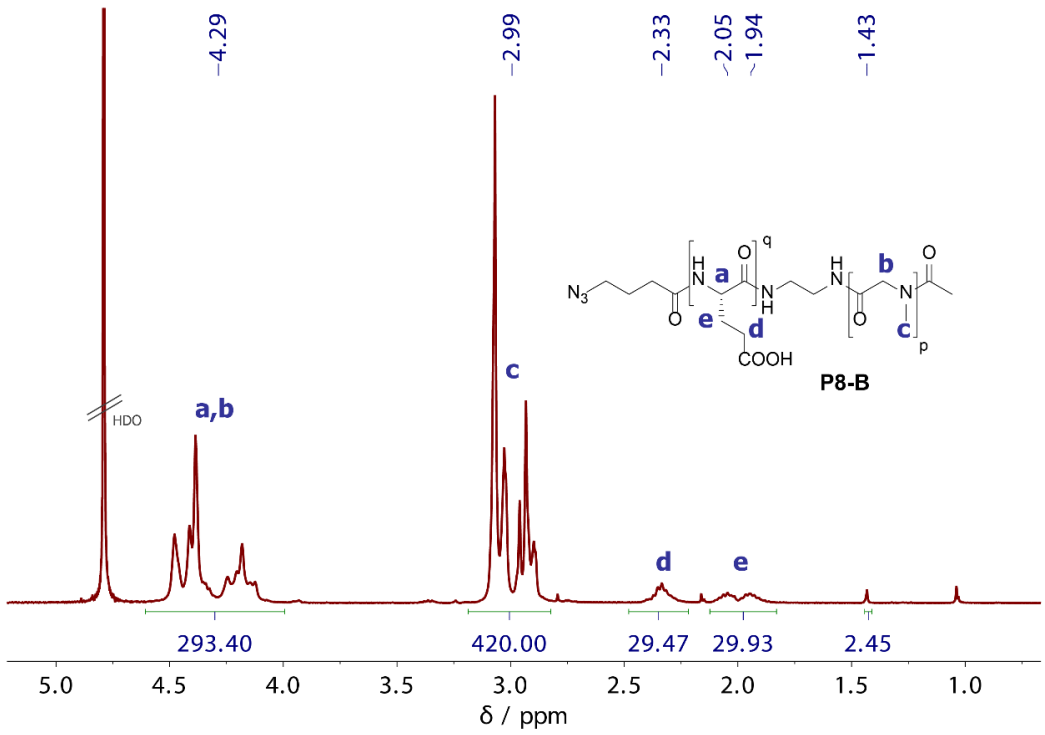

Figure S25. ^{1}H NMR spectrum of **P8-B** ($pSar_{140}$-*b*-$pGlu(OH)_{15}$) in D_2O.

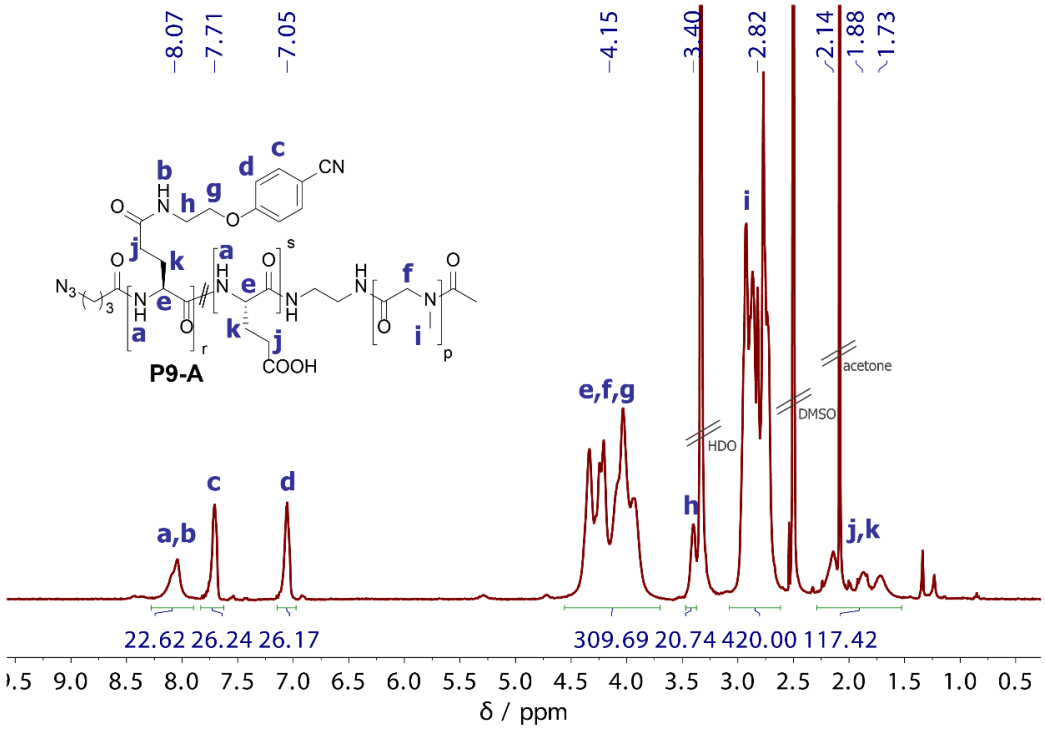

Figure S26. ^{1}H NMR spectrum of **P9-A** ($pSar_{140}$-*b*-$pGlu(Mod)_{20}$) in DMSO-d_6.

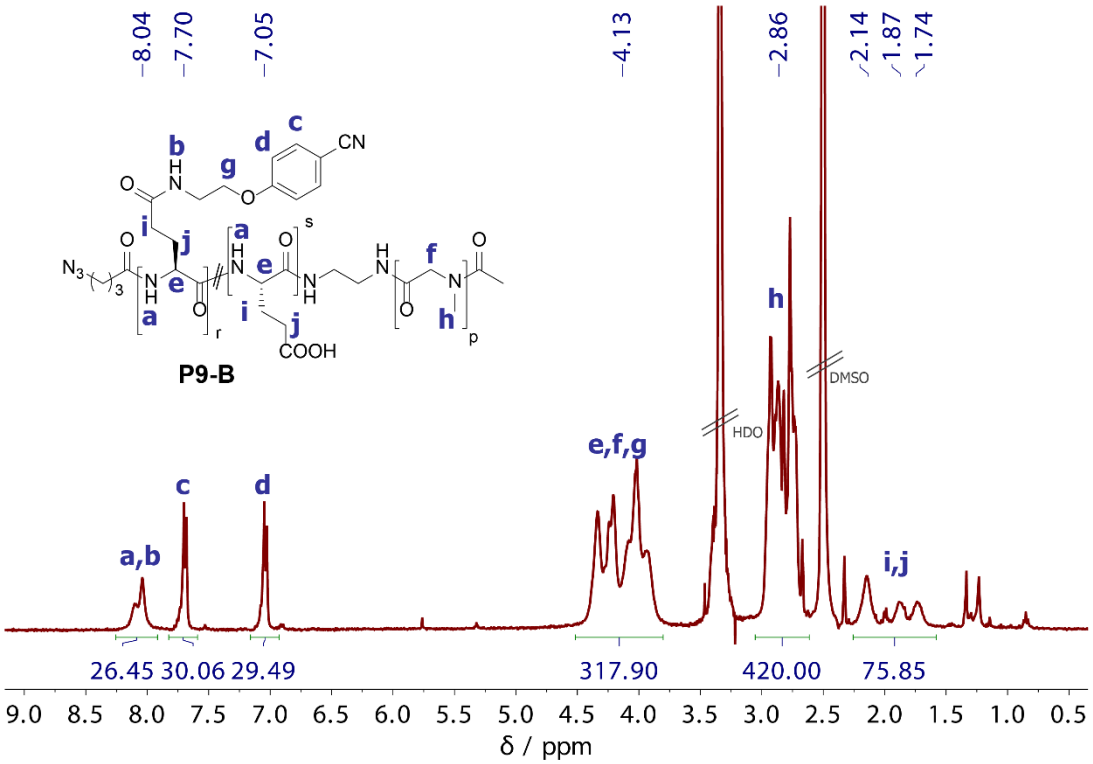

Figure S27. ^{1}H NMR spectrum of **P9-B** (pSar$_{140}$-*b*-pGlu(Mod)$_{15}$) in DMSO-d_6.

DOSY NMR Spectra

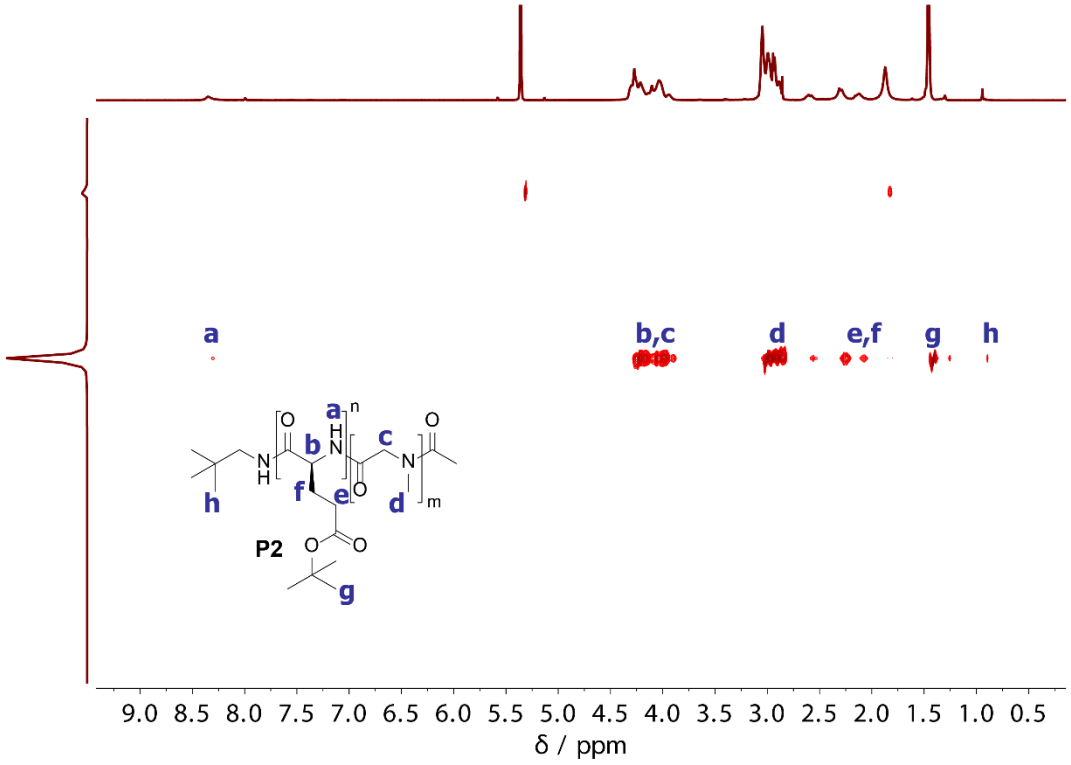

Figure S28. DOSY NMR spectrum of **P2** (pGlu(O*t*Bu)$_{36}$-*b*-pSar$_{171}$) in CD_2Cl_2.

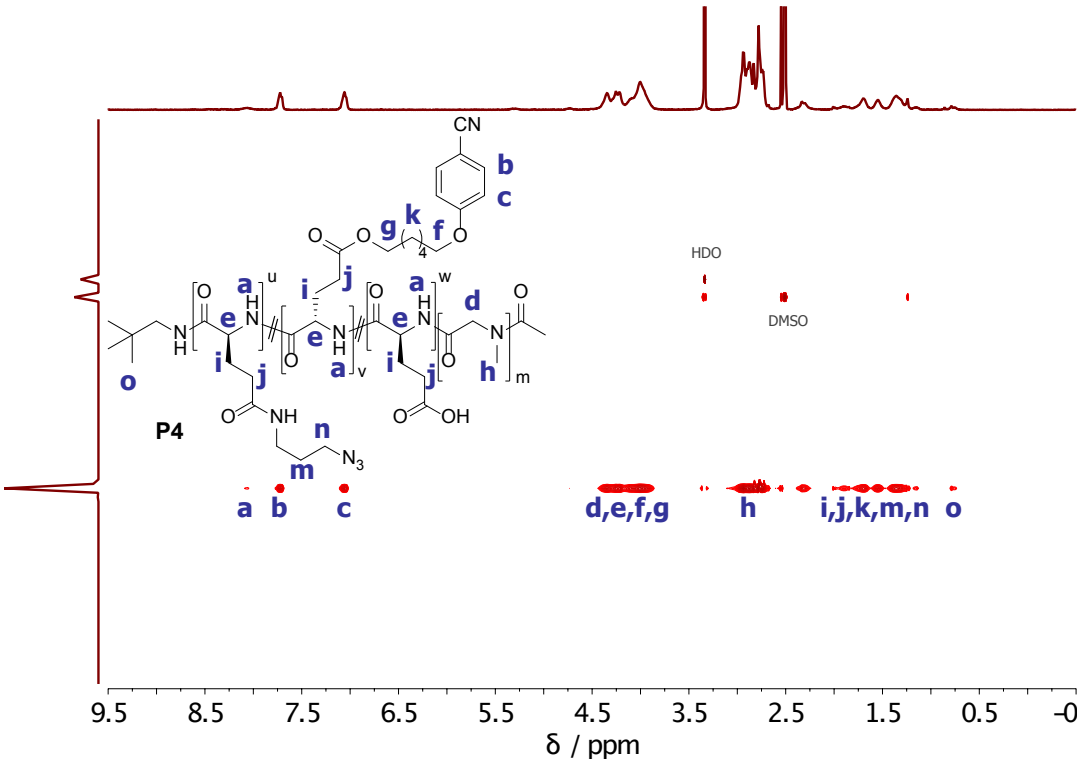

Figure S29. DOSY NMR spectrum of **P4** (pGlu(Mod)$_{36}$-*b*-pSar$_{171}$) in DMSO-d_6.

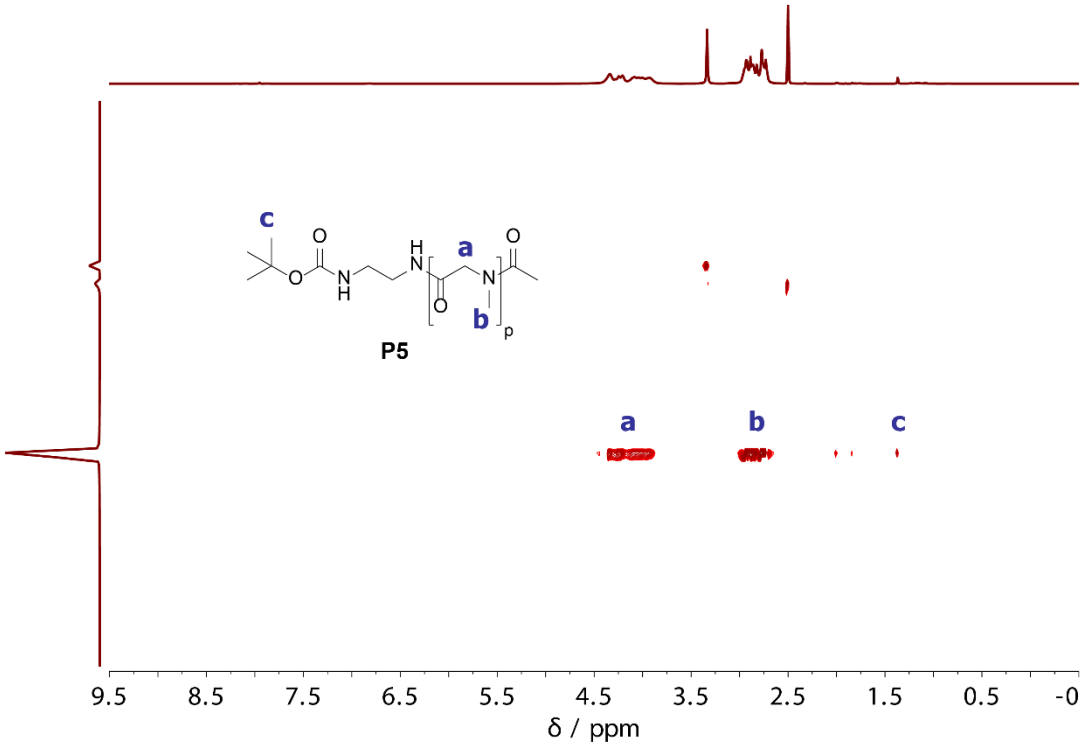

Figure S30. DOSY NMR spectrum of **P5** (*N*-Boc-pSar$_{140}$) in DMSO-d_6.

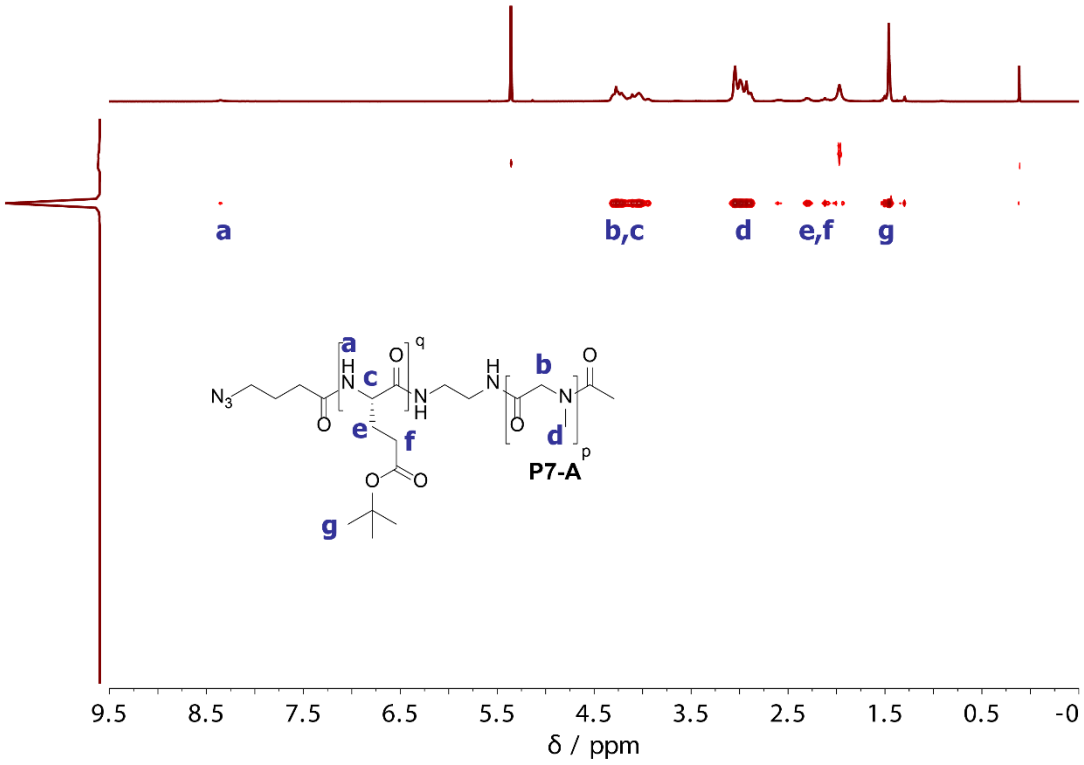

Figure S31. DOSY NMR spectrum of **P7-A** (pSar$_{140}$-*b*-pGlu(O*t*Bu)$_{20}$) in CD_2Cl_2.

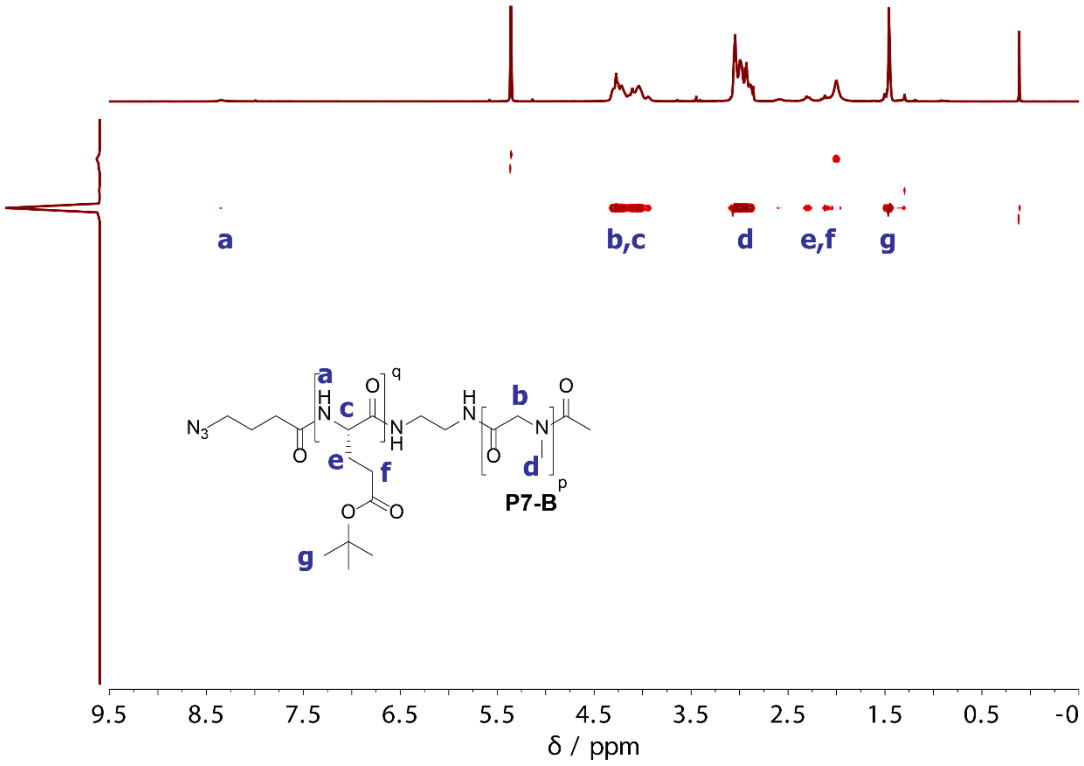

Figure S32. DOSY NMR spectrum of **P7-B** ($pSar_{140}$-*b*-$pGlu(O\mathit{t}Bu)_{15}$) in CD_2Cl_2.

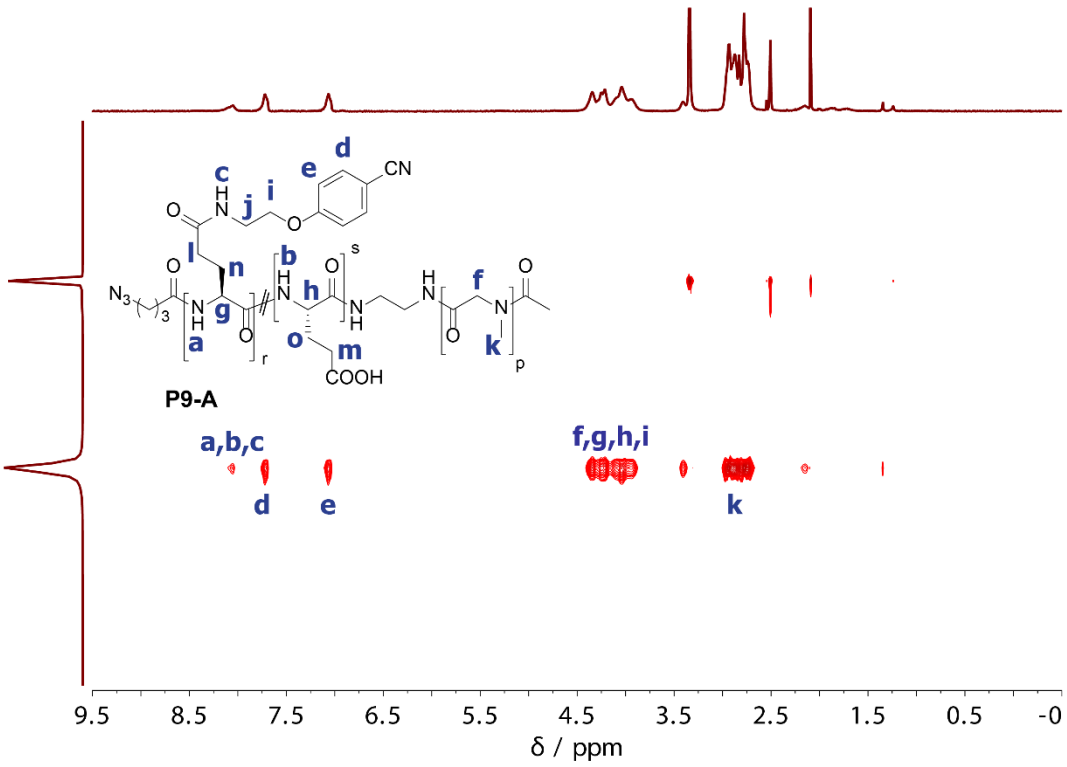

Figure S33. DOSY NMR spectrum of **P9-A** ($pSar_{140}$-*b*-$pGlu(Mod)_{20}$) in DMSO-d_6.